Auton Robot (2016) 40:505–517
DOI 10.1007/s10514-015-9438-z

Whole-body impedance control of wheeled mobile manipulators

Stability analysis and experiments on the humanoid robot Rollin' Justin

Alexander Dietrich[1] · **Kristin Bussmann**[1] · **Florian Petit**[1] · **Paul Kotyczka**[2] · **Christian Ott**[1] · **Boris Lohmann**[2] · **Alin Albu-Schäffer**[1,3]

Received: 7 August 2014 / Accepted: 12 May 2015 / Published online: 26 May 2015

Abstract Humanoid service robots in domestic environments have to interact with humans and their surroundings in a safe and reliable way. One way to manage that is to equip the robotic systems with force-torque sensors to realize a physically compliant whole-body behavior via impedance control. To provide mobility, such robots often have wheeled platforms. The main advantage is that no balancing effort has to be made compared to legged humanoids. However, the nonholonomy of most wheeled systems prohibits the direct implementation of impedance control due to kinematic rolling constraints that must be taken into account in modeling and control. In this paper we design a whole-body impedance controller for such a robot, which employs an admittance interface to the kinematically controlled mobile platform. The upper body impedance control law, the platform admittance interface, and the compensation of dynamic couplings between both subsystems yield a passive closed loop. The convergence of the state to an invariant set is shown. To prove asymptotic stability in the case of redundancy, priority-based approaches can be employed. In principle, the presented approach is the extension of the well-known and established impedance controller to mobile robots. Experimental validations are performed on the humanoid robot Rollin' Justin. The method is suitable for compliant manipulation tasks with low-dimensional planning in the task space.

Keywords Whole-body control · Impedance control · Admittance control · Humanoid robots · Mobile manipulation · Stability analysis

Electronic supplementary material The online version of this article (doi:10.1007/s10514-015-9438-z) contains supplementary material, which is available to authorized users.

✉ Alexander Dietrich
alexander.dietrich@dlr.de

[1] Institute of Robotics and Mechatronics, German Aerospace Center (DLR), Muenchner Strasse 20, 82234 Wessling, Germany

[2] Institute of Automatic Control, Technische Universität München (TUM), Boltzmannstrasse 15, 85748 Garching, Germany

[3] Sensor-Based Robotic Systems and Intelligent Assistance Systems, Technische Universität München (TUM), Boltzmannstrasse 3, 85748 Garching, Germany

1 Introduction

Robots in industrial applications are usually caged and mostly restricted to workspaces where the presence of humans is excluded. The next step towards domestic applications in households and human environments requires massive adaptation and effort to make future service robots safe and reliable. A central point in this context is to make the robots compliant w. r. t. their environment. Beside using particular mechanics such as passive springs to provide soft behavior (Ham et al. 2009; Siciliano and Khatib 2008), the concept of active compliance (Hogan 1985) is a well established robot control technology. Elaborate compliant whole-body control concepts have been developed starting with theoretical investigations and simulations (Khatib et al. 2004; Sentis and Khatib 2005). By now these techniques are more and more applied and validated on real hardware (Nagasaka et al. 2010; Dietrich et al. 2012b; Moro et al. 2013). However, formal stability analyses do not exist.

Humanoid robots are predestined to be employed in service robotic environments since households (rooms, tools, geometries) are specifically designed for humans, e. g. two-handed manipulation and human dimensions. In the last decade, a wide variety of different systems have been devel-

oped: HRP-4 (Kaneko et al. 2011), ASIMO (Sakagami et al. 2002), ARMAR-III (Asfour et al. 2006), TWENDY-ONE (Iwata and Sugano 2009), LOLA (Lohmeier et al. 2009), Rollin' Justin (Borst et al. 2009), PR2 (Bohren et al. 2011), just to name a few. One can classify these robots w. r. t. their kind of locomotion. On the one hand, there are legged systems such as HRP-4 or ASIMO, and on the other hand, wheeled humanoid robots such as TWENDY-ONE or Rollin' Justin have been designed. Up to now many complex service tasks have been executed by wheeled robots only. The advantage of most of these mobile bases (excluding platforms with less than three wheels (Stilman et al. 2010)) is to focus on sophisticated manipulation skills without the necessity of making large efforts for balancing and stabilizing the gait. Based on these considerations we expect that wheeled systems will occupy an important place in future service robotics. We have already shown that whole-body impedance frameworks applied to wheeled humanoid robots give promising results (Dietrich et al. 2011a, 2012b). However, the nonholonomy of the mobile platform requires to handle the kinematic rolling constraints for consistent locomotion. An admittance coupling can be used to integrate the base into the whole-body framework on force-torque level. However, experiments revealed that the parameterization of the whole-body impedance and the platform admittance are restricted such that conservative gains must be chosen to preserve stability. That significantly degrades the performance of the method in turn.

In this article we will present a new whole-body controller and verify that the mentioned robustness problems are due to inertia and Coriolis/centrifugal couplings between the upper body and the mobile base. The closed-loop passivity allows for a proof of asymptotic stability of the desired equilibrium. Compared to the standard concept (Dietrich et al. 2011a, 2012b), the performance of the whole-body controller is superior while ensuring stability at the same time. Experiments on the humanoid robot Rollin' Justin (Fig. 1) validate the approach.

The remainder of this paper is organized as follows: After a brief introduction to the dynamics representation of the robot in Sect. 2, the control of the subsystems (platform, upper body) is explained in Sect. 3. The whole-body impedance controller and the formal stability analysis are presented in Sect. 4. Comparative experiments in Sect. 5 confirm our theoretical results on Rollin' Justin. The discussion of the approach in Sect. 6 closes the paper.

2 Fundamentals

This section briefly recapitulates rigid robot dynamics (Sect. 2.1) and restricts it to nonholonomic, wheeled robots (Sect. 2.2) for later use in the succeeding analysis.

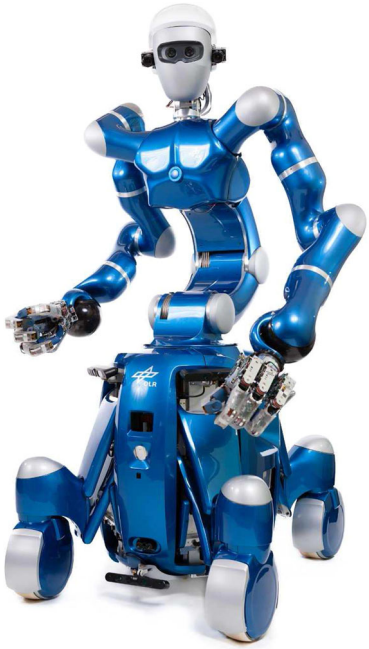

Fig. 1 The humanoid robot Rollin' Justin: its upper body with 43 actuated DOF is torque-controlled (except for the two neck joints), the mobile base with eight actuated DOF is position/velocity-controlled

2.1 General rigid robot dynamics

The dynamic equations of a fully actuated robot with n DOF (degrees of freedom) and joint coordinates $\boldsymbol{\theta} \in \mathbb{R}^n$ can be written as

$$\mathbf{M}(\boldsymbol{\theta})\ddot{\boldsymbol{\theta}} + \mathbf{C}(\boldsymbol{\theta}, \dot{\boldsymbol{\theta}})\dot{\boldsymbol{\theta}} + \mathbf{g}(\boldsymbol{\theta}) = \boldsymbol{\tau} + \boldsymbol{\tau}^{\text{ext}} . \tag{1}$$

The inertia matrix $\mathbf{M}(\boldsymbol{\theta}) \in \mathbb{R}^{n\times n}$ is symmetric and positive definite. Gravity forces and torques are taken into account by $\mathbf{g}(\boldsymbol{\theta}) = (\partial V_{\text{g}}(\boldsymbol{\theta})/\partial\boldsymbol{\theta})^T \in \mathbb{R}^n$, where $V_{\text{g}}(\boldsymbol{\theta})$ denotes the gravity potential. Joint forces and torques are represented by $\boldsymbol{\tau} \in \mathbb{R}^n$ and external forces and torques are denoted by $\boldsymbol{\tau}^{\text{ext}} \in \mathbb{R}^n$.[1] Coriolis and centrifugal effects are included in $\mathbf{C}(\boldsymbol{\theta}, \dot{\boldsymbol{\theta}})\dot{\boldsymbol{\theta}} \in \mathbb{R}^n$. This term complies with

$$\dot{\mathbf{M}}(\boldsymbol{\theta}, \dot{\boldsymbol{\theta}}) = \mathbf{C}(\boldsymbol{\theta}, \dot{\boldsymbol{\theta}}) + \mathbf{C}(\boldsymbol{\theta}, \dot{\boldsymbol{\theta}})^T \tag{2}$$

which is equivalent to the skew symmetry of $\dot{\mathbf{M}}(\boldsymbol{\theta}, \dot{\boldsymbol{\theta}}) - 2\mathbf{C}(\boldsymbol{\theta}, \dot{\boldsymbol{\theta}})$. This property is crucial for showing passivity of (1) w. r. t. input $\boldsymbol{\tau}$ and output $\dot{\boldsymbol{\theta}}$ and the total energy $\frac{1}{2}\dot{\boldsymbol{\theta}}^T\mathbf{M}(\boldsymbol{\theta})\dot{\boldsymbol{\theta}} + V_{\text{g}}(\boldsymbol{\theta})$ as the storage function (Murray et al. 1994).

[1] Since most manipulators are rather equipped with revolute joints than prismatic joints, we refer to *joint torques* in this paper. Nevertheless, the generalization to joint forces and joint torques can be made without loss of generality.

2.2 Robots with wheeled, nonholonomic mobile platforms

The dynamics (1) can also be formulated for robots with nonholonomic, wheeled mobile platforms under kinematic rolling constraints. In the literature (Campion et al. 1996; Siciliano and Khatib 2008), an undercarriage such as the platform of Rollin' Justin is called of "type (1,2)" with a *maneuverability* of dimension $\delta_m = 1$, and a *steerability* of dimension $\delta_s = 2$. The analysis of this kind of system is a standard issue in robotics and will not be performed here. For a detailed investigation of the kinematic and dynamic properties see Siciliano and Khatib (2008). Nonetheless, we want to point out a few important properties which can be concluded for type (1,2) platforms and apply them to the mobile base of Rollin' Justin.

1. Although the base cannot change its direction of motion instantaneously, it is able to move freely in the plane by adjusting the wheels (steering and propulsion) appropriately.
2. The mobile platform has basically three DOF for the overall motion, which are: the translation forward/backward, the translation left/right, and the rotation about the vertical axis. In the following, we denote the respective coordinates as $\mathbf{r} \in \mathbb{R}^3$.
3. The platform is dynamically feedback linearizable. Giordano et al. (2009) have already implemented a controller, which allows to command a desired trajectory $\mathbf{r}^{\mathrm{des}}(t)$ w. r. t. time t. An underlying wheel velocity controller is then employed to realize the coordinated wheel behavior (steering and propulsion).

In the following section, the mobile base control framework will be presented. Afterwards, the upper body control framework will be detailed.

3 Subsystem control

An increasing number of humanoid robots is equipped with torque sensors in the upper body joints. That allows to implement torque control techniques to realize a compliant interaction behavior, e. g. by applying impedance-based laws (Hogan 1985; Albu-Schäffer et al. 2007; Ott 2008). However, nonholonomic platforms require algorithms to solve the kinematic rolling constraints. These constraints are usually fulfilled from a kinematic perspective by suitable velocity controllers (Thuilot et al. 1996; Asfour et al. 2006; Connette et al. 2008; Giordano et al. 2009). For that reason, a force-torque-based whole-body impedance framework cannot be applied to such systems in a straightforward way. The velocity-controlled subsystems have to be made accessible by an additional *admittance interface* to transform desired forces and torques into applicable motion trajectories.

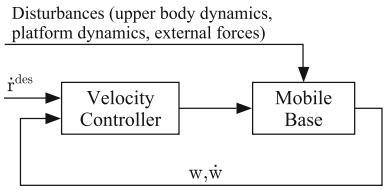

Fig. 2 Control loop of the velocity controller for the mobile platform. The control gains are high to compensate for any disturbances as depicted

The velocity controller of the mobile base of Rollin' Justin is briefly reviewed in Sect. 3.1. Afterwards, the admittance interface is presented in Sect. 3.2. These two subsystems are interconnected such that their interconnection has a virtual force-torque input. The resulting equations of motion of the wheeled platform and the upper body dynamics are explained in Sect. 3.3. Sections 3.4 and 3.5 present the task space impedance controller and demonstrate stability problems which arise when the impedance control law is applied to the complete robot (via the admittance in the platform) without modifications.

3.1 Mobile base velocity control

As mentioned above, a dynamic feedback linearization can be applied to the platform of Rollin' Justin. In combination with an underlying, high-gain wheel velocity controller, one is able to realize arbitrary desired trajectories in the coordinates $\mathbf{r}$, while the kinematic rolling constraints (*Pfaffian constraints*) are automatically satisfied. The corresponding control structure is illustrated in Fig. 2. Herein, the *Velocity Controller* block includes both the dynamic feedback linearization (Giordano et al. 2009) and the underlying high-gain wheel velocity controller. The signals $\mathbf{w}$ and $\dot{\mathbf{w}}$ denote the wheel positions (steering and propulsion) and wheel velocities, respectively. A major feature of the controller is that it compensates for any disturbances due to the high gains. These disturbances are primarily due to dynamic couplings between the upper body of the robot and the mobile base. Moreover, external forces/torques and dynamic effects of the platform itself are compensated for.

Summarized, the sketched platform velocity control framework allows the assumption $\dot{\mathbf{r}} \approx \dot{\mathbf{r}}^{\mathrm{des}}$, while the desired trajectory $\dot{\mathbf{r}}^{\mathrm{des}}$ may be arbitrary as long as it is smooth (twice differentiable).

3.2 Admittance interface to mobile base

Using the velocity control framework from above, we are free to command desired (virtual) base dynamics, which the

platform is supposed to follow. Since our main goal is to implement a whole-body impedance control law, a force-torque interface is favored.

In this respect, we design an admittance simulation with virtual platform inertia and virtual damping:

$$\mathbf{M}_{\text{adm}}\ddot{\mathbf{r}}^{\text{des}} + \mathbf{D}_{\text{adm}}\dot{\mathbf{r}}^{\text{des}} = \boldsymbol{\tau}_{\text{r}}^{\text{virt}} + \boldsymbol{\tau}_{\text{r}}^{\text{ext}} \tag{3}$$

where $\boldsymbol{\tau}_{\text{r}}^{\text{virt}} \in \mathbb{R}^3$ is a virtual force/torque that can be used as the control input (commanded by the whole-body impedance controller) to generate the simulated velocity profile $\dot{\mathbf{r}}^{\text{des}}$. External forces/torques $\boldsymbol{\tau}_{\text{r}}^{\text{ext}} \in \mathbb{R}^3$ can only be used in the admittance if the platform is equipped with appropriate sensor capabilities. If no sensors are available, $\boldsymbol{\tau}_{\text{r}}^{\text{ext}}$ has to be set to zero in (3) although external loads may exist physically. Note again that the underlying velocity controller compensates for any disturbances, and $\boldsymbol{\tau}_{\text{r}}^{\text{ext}}$ belongs to this category. In other words, if $\boldsymbol{\tau}_{\text{r}}^{\text{ext}}$ is not measured, the mobile platform will be insensitive w. r. t. external forces and torques exerted there. The parameters $\mathbf{M}_{\text{adm}}$ and $\mathbf{D}_{\text{adm}}$ represent the virtual inertia and damping of the admittance simulation, respectively. A reasonable choice for these values is

$$\begin{aligned}\mathbf{M}_{\text{adm}} &= \text{diag}(m_{\text{adm},1}, m_{\text{adm},2}, m_{\text{adm},3}) && (4)\\ &= \text{diag}(m, m, I), && (5)\\ \mathbf{D}_{\text{adm}} &= \text{diag}(d_{\text{adm},1}, d_{\text{adm},2}, d_{\text{adm},3}), && (6)\end{aligned}$$

where $m \in \mathbb{R}^+$ is the virtual platform mass and $I \in \mathbb{R}^+$ is the virtual moment of inertia. One can specify a decoupled damping to determine the positive definite matrix via $d_{\text{adm},i}$ for $i = 1 \ldots 3$. The advantages of the formulation (3) are discussed in the following. A first-order low-pass filter can be described in the Laplace domain as

$$sR_i^{\text{des}}(s) = \frac{K_i}{T_i s + 1}\left(\tau_{\text{r},i}^{\text{virt}}(s) + \tau_{\text{r},i}^{\text{ext}}\right), \tag{7}$$

$$K_i = \frac{1}{d_{\text{adm},i}}, \quad T_i = \frac{m_{\text{adm},i}}{d_{\text{adm},i}}. \tag{8}$$

Here, $R_i^{\text{des}}(s)$ is the Laplace transform of the ith element in $\mathbf{r}^{\text{des}}$, $\tau_{\text{r},i}^{\text{virt}}(s)$ and $\tau_{\text{r},i}^{\text{ext}}$ are the Laplace transforms of the ith element in $\boldsymbol{\tau}_{\text{r}}^{\text{virt}}$ and $\boldsymbol{\tau}_{\text{r}}^{\text{ext}}$, respectively. Based on (8) we can parameterize the admittance simulation in an intuitive way. First, we choose the inertia parameters $m_{\text{adm},i}$ for $i = 1 \ldots 3$, i. e. the inertia of the platform which is supposed to be perceived. Second, we parameterize the gains K_i for $i = 1 \ldots 3$. The whole-body impedance controller delivers the maximum desired forces/torques (down to the platform). Via K_i, we can directly compute the respective maximum admittance velocity. That way, we restrict the base velocities for safety. The reason behind limited forces/torques from the whole-body impedance controller is that an excessive error between the actual and the desired TCP (tool center point) position/orientation may not lead to unfeasible control inputs.

Note again that the admittance (3) does *not* represent a real physical system but it is only a simulated, desired dynamic behavior we would like the platform to show. In other words, if the admittance mass is set to 10 kg, then the platform behaves like it only weighs 10 kg although its real mass amounts to about 150 kg.

3.3 Overall dynamics

Under the assumption of Sect. 3.1, i. e. $\dot{\mathbf{r}} \approx \dot{\mathbf{r}}^{\text{des}}$, the overall dynamics can be formulated as

$$\begin{pmatrix}\mathbf{M}_{\text{adm}} & \mathbf{0}\\ \mathbf{M}_{\text{qr}} & \mathbf{M}_{\text{qq}}\end{pmatrix}\begin{pmatrix}\ddot{\mathbf{r}}\\ \ddot{\mathbf{q}}\end{pmatrix} + \begin{pmatrix}\mathbf{D}_{\text{adm}} & \mathbf{0}\\ \mathbf{C}_{\text{qr}} & \mathbf{C}_{\text{qq}}\end{pmatrix}\begin{pmatrix}\dot{\mathbf{r}}\\ \dot{\mathbf{q}}\end{pmatrix} + \begin{pmatrix}\mathbf{0}\\ \mathbf{g}_{\text{q}}\end{pmatrix} = \begin{pmatrix}\boldsymbol{\tau}_{\text{r}}^{\text{virt}}\\ \boldsymbol{\tau}_{\text{q}}\end{pmatrix} + \begin{pmatrix}\boldsymbol{\tau}_{\text{r}}^{\text{ext}}\\ \boldsymbol{\tau}_{\text{q}}^{\text{ext}}\end{pmatrix}. \tag{9}$$

The first line represents (3), while the second line describes the upper body dynamics with joint configuration $\mathbf{q} \in \mathbb{R}^{n_{\text{q}}}$ for n_{q} upper body joint variables. Herein, $\mathbf{M}_{\text{qq}}$ is the respective upper body inertia matrix and $\mathbf{M}_{\text{qr}}$ is the inertia coupling to the mobile base. Accordingly, $\mathbf{C}_{\text{qr}}$ and $\mathbf{C}_{\text{qq}}$ denote the corresponding Coriolis/centrifugal terms. All upper body gravity torques are contained in $\mathbf{g}_{\text{q}}$. The torques $\boldsymbol{\tau}_{\text{q}}$ are considered as the control inputs to the upper body and $\boldsymbol{\tau}_{\text{q}}^{\text{ext}}$ are the external torques. Dependencies on the states are omitted in the notations of (9). For later use, we define the vector

$$\mathbf{y} = \begin{pmatrix}\mathbf{r}\\ \mathbf{q}\end{pmatrix}, \tag{10}$$

which describes the configuration of the robot. Herein the mobile platform is only represented by its Cartesian position $\mathbf{r}$, while the wheel positions and steering angles $\mathbf{w}$ are not represented. Thus, (10) is only a reduced configuration description, but it defines the DOF which the whole-body impedance controller will finally access. Before introducing the impedance law, the properties of the dynamics (9) are summarized:

1. A high-gain velocity controller is used to fulfill the rolling constraints and to realize the desired admittance dynamics (3) for the mobile base. All disturbances, including the dynamic coupling forces/torques from the upper body, are assumed to be compensated properly by this controller (cf. Fig. 2).
2. The term $\boldsymbol{\tau}_{\text{r}}^{\text{virt}}$ can be used as the control input for the mobile platform.
3. The term $\boldsymbol{\tau}_{\text{q}}$ can be used as the control input for the upper body joints.

4. The properties of the dynamics (9) do not comply with the standard formulation (1) any longer, e. g. the inertia matrix is not symmetric and (2) cannot be concluded from (9) anymore.

3.4 Impedance control in the operational space

A spatial impedance can be designed in the operational space such as the Cartesian space of the TCP. The desired TCP behavior is implemented by applying the impedance to the complete system so that overall compliance w. r. t. the TCP is achieved. The spatial error $\tilde{\mathbf{x}} \in \mathbb{R}^{n_x}$ in the operational space is given by

$$\tilde{\mathbf{x}}(\mathbf{y}) = \mathbf{x}(\mathbf{y}) - \mathbf{x}^{\text{des}}, \tag{11}$$

where n_x is the dimension of the operational space (for Cartesian impedance: $n_x = 6$), $\mathbf{x}(\mathbf{y})$ describes the forward kinematics and $\mathbf{x}^{\text{des}}$ is the desired TCP position/orientation. The positive definite, virtual potential $V_{\text{imp}}(\tilde{\mathbf{x}}(\mathbf{y}))$ represents the spatial spring which may be of the form

$$V_{\text{imp}}(\tilde{\mathbf{x}}(\mathbf{y})) = \frac{1}{2}\tilde{\mathbf{x}}(\mathbf{y})^T \mathbf{K}\tilde{\mathbf{x}}(\mathbf{y}) \tag{12}$$

for a positive definite stiffness matrix $\mathbf{K} \in \mathbb{R}^{n_x \times n_x}$. One can compute the control torques from the spring potential and the upper body damping as

$$\boldsymbol{\tau}_{\text{imp}} = -\left(\frac{\partial V_{\text{imp}}(\tilde{\mathbf{x}}(\mathbf{y}))}{\partial \mathbf{y}}\right)^T, \tag{13}$$

$$\boldsymbol{\tau}_{\text{damp}} = -\begin{pmatrix} \mathbf{0} \\ \mathbf{D}_{\text{qq}}\dot{\mathbf{q}} \end{pmatrix}, \tag{14}$$

yielding the control input

$$\begin{pmatrix} \boldsymbol{\tau}_{\text{r}}^{\text{virt}} \\ \boldsymbol{\tau}_{\text{q}} \end{pmatrix} = \boldsymbol{\tau}_{\text{imp}} + \boldsymbol{\tau}_{\text{damp}}. \tag{15}$$

The damping matrix $\mathbf{D}_{\text{qq}} \in \mathbb{R}^{n_q \times n_q}$ has to be positive definite. Damping w. r. t. the platform subsystem has already been injected by the admittance in Sect. 3.2. In Sect. 4, the overall damping matrix $\bar{\mathbf{D}}$ will be introduced, which contains the upper body and the platform damping. The impedance torque $\boldsymbol{\tau}_{\text{imp}}$ consists of n_q elements related to the upper body and $n_r = 3$ elements related to the mobile base. The upper body torques are directly applied and commanded to the torque controllers in the joints via $\boldsymbol{\tau}_q$. The platform forces/torques in $\boldsymbol{\tau}_{\text{imp}}$ are commanded as $\boldsymbol{\tau}_{\text{r}}^{\text{virt}}$ in the admittance (3).

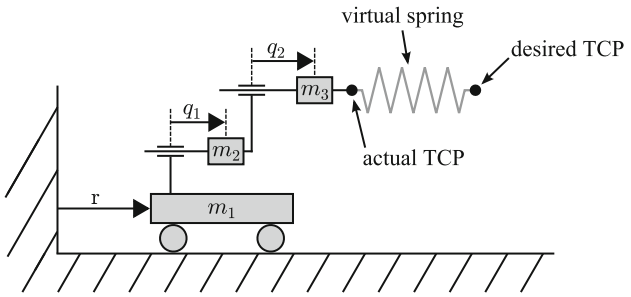

Fig. 3 Linear simulation model with three DOF

Table 1 Parameters for the simulation of the three DOF robot

Parameter	Value	Unit
m_1, m_2, m_3	1	kg
$\mathbf{K}$	1	N/m
$\mathbf{D}_{\text{qq}}$	diag(1, 1)	kg/s

Table 2 Elements of the system matrix $\mathbf{A}$

Row\col.	r	q_1	q_2	$\dot{r}$	$\dot{q}_1$	$\dot{q}_2$
$\dot{r}$	0	0	0	1	0	0
$\dot{q}_1$	0	0	0	0	1	0
$\dot{q}_2$	0	0	0	0	0	1
$\ddot{r}$	$-1/m_{\text{adm}}$	$-1/m_{\text{adm}}$	$-1/m_{\text{adm}}$	$-d_{\text{adm}}/m_{\text{adm}}$	0	0
$\ddot{q}_1$	$1/m_{\text{adm}}$	$1/m_{\text{adm}}$	$1/m_{\text{adm}}$	$d_{\text{adm}}/m_{\text{adm}}$	-1	1
$\ddot{q}_2$	-1	-1	-1	0	1	-2

The units are omitted in the notations

3.5 Interaction between torque-controlled upper body and admittance-controlled platform on a 3 DOF system

In this section a linear three DOF system will be analyzed to demonstrate the stability problems arising when (9) is used together with the whole-body impedance (15). The manipulator is sketched in Fig. 3. The system parameters and the controller parameterization are given in Table 1. The dynamics can be analyzed using standard methods from linear control theory. The closed-loop dynamics can be represented as a continuous, time-invariant state-space model $\dot{\mathbf{z}} = \mathbf{A}\mathbf{z} + \mathbf{B}\mathbf{u}$, where $\mathbf{z} = (r, q_1, q_2, \dot{r}, \dot{q}_1, \dot{q}_2)^T$ is the state vector, $\mathbf{A}$ defines the closed-loop poles (system matrix), and the input is defined by the input matrix $\mathbf{B}$ and the input vector $\mathbf{u}$. The stability properties are determined by $\mathbf{A}$, whose elements are shown in Table 2.

Different parameterizations of the virtual platform mass m_{adm} and damping d_{adm} have been applied and the maximum real part of all closed-loop poles has been evaluated. Figure 4 shows where this value is larger than zero (unstable system) and where it is negative (stable system). The instability orig-

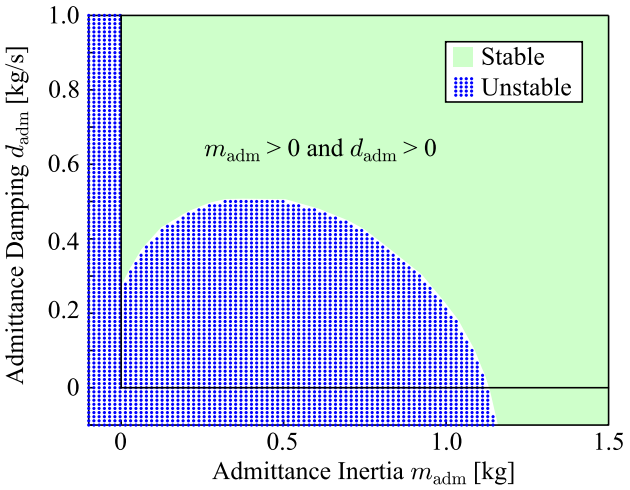

Fig. 4 Stable and unstable closed-loop poles of the linear three DOF robot depending on the admittance parameterization. Inertia couplings exist, i. e. $\mathbf{M}_{\text{qr}} \neq \mathbf{0}$. No Coriolis/centrifugal terms exist due to the use of prismatic joints, i. e. $\mathbf{C}_{\text{qr}} = \mathbf{0}$

inates from the inertia coupling $\mathbf{M}_{\text{qr}}$ (9) between upper body and mobile base.

When the system is analyzed with active compensation of the coupling $\mathbf{M}_{\text{qr}}$, stability is ensured for *all* reasonable parameterizations $m_{\text{adm}} > 0$, $d_{\text{adm}} > 0$. In this case the elements in $\mathbf{A}$, located in row/column 5/1, 5/2, 5/3 and 5/4, are zero, cf. elements in Table 2. Then the resulting inertia matrix is positive definite, while this is not the case if the coupling $\mathbf{M}_{\text{qr}}$ is uncompensated.

Albeit only analyzed for a linear system here, we have experienced similar effects on Rollin' Justin during our experiments. Such an instability scenario due to the coupling is demonstrated in the video. On Rollin' Justin, one has Coriolis and centrifugal couplings additionally, thus $\mathbf{C}_{\text{qr}} \neq \mathbf{0}$.

4 Whole-body impedance controller and proof of stability

In Sect. 3.5 it was shown that the inertia and Coriolis/centrifugal couplings between admittance-controlled mobile base and torque-controlled upper body can destabilize the system. In this section, the compensation of these couplings in combination with the whole-body control framework and a proof of stability for the closed loop are presented.

4.1 Controller

Based on the insights from Sect. 3.5, the inertia matrix has to be decoupled such that it becomes symmetric again. Therefore, the impedance control law (15) is extended by an additional compensation term:

$$\begin{pmatrix} \boldsymbol{\tau}_{\text{r}}^{\text{virt}} \\ \boldsymbol{\tau}_{\text{q}} \end{pmatrix} = \boldsymbol{\tau}_{\text{imp}} + \boldsymbol{\tau}_{\text{damp}} + \boldsymbol{\tau}_{\text{comp}}, \tag{16}$$

$$\boldsymbol{\tau}_{\text{comp}} = \begin{pmatrix} \mathbf{0} \\ \mathbf{M}_{\text{qr}}\ddot{\mathbf{r}} + \mathbf{C}_{\text{qr}}\dot{\mathbf{r}} + \mathbf{g}_{\text{q}} \end{pmatrix}. \tag{17}$$

The compensation action $\boldsymbol{\tau}_{\text{comp}}$ brings the dynamics into the standard form of rigid robot dynamics (cf. Sect. 2.1) such that the resulting inertia matrix is symmetric and positive definite, and the property (2) holds again. The accelerations $\ddot{\mathbf{r}}$ do not have to be measured, they can be taken from the admittance simulation (3) due to the assumption $\dot{\mathbf{r}} \approx \dot{\mathbf{r}}^{\text{des}}$. Thus

$$\ddot{\mathbf{r}} \approx \ddot{\mathbf{r}}^{\text{des}} = \mathbf{M}_{\text{adm}}^{-1} \left(\boldsymbol{\tau}_{\text{r}}^{\text{virt}} + \boldsymbol{\tau}_{\text{r}}^{\text{ext}} - \mathbf{D}_{\text{adm}} \dot{\mathbf{r}}^{\text{des}} \right). \tag{18}$$

The controller structure on Rollin' Justin is sketched in Fig. 5.

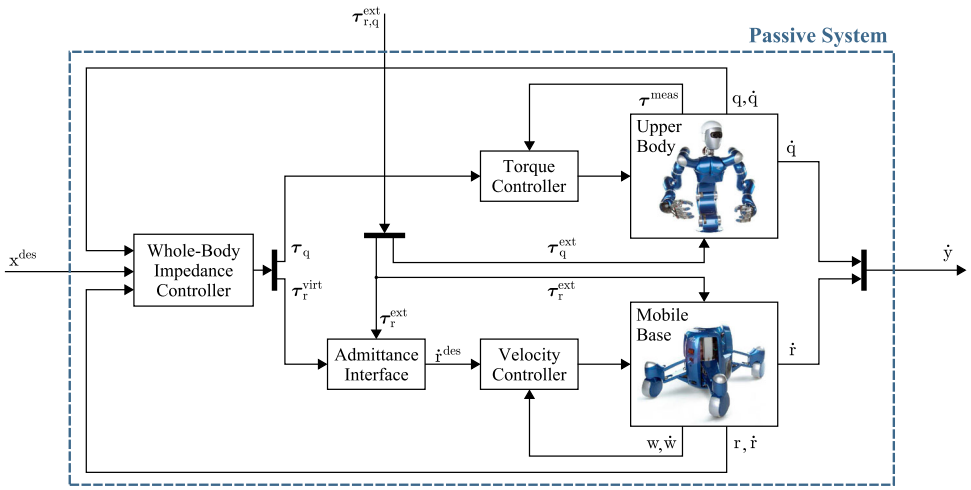

Fig. 5 Whole-body impedance control with the humanoid robot Rollin' Justin. The closed loop is passive w. r. t. the input $\boldsymbol{\tau}_{\text{r,q}}^{\text{ext}}$ and the output $\dot{\mathbf{y}}$. The measured upper body joint torques are denoted by $\boldsymbol{\tau}^{\text{meas}}$

4.2 Stability analysis

With the proposed controller (16), the dynamic equations take the form

$$\bar{\mathbf{M}}\ddot{\mathbf{y}} + \bar{\mathbf{C}}\dot{\mathbf{y}} + \bar{\mathbf{D}}\dot{\mathbf{y}} = \boldsymbol{\tau}_{\text{imp}} + \boldsymbol{\tau}_{\text{r,q}}^{\text{ext}} \tag{19}$$

with

$$\bar{\mathbf{M}} = \begin{pmatrix} \mathbf{M}_{\text{adm}} & \mathbf{0} \\ \mathbf{0} & \mathbf{M}_{\text{qq}} \end{pmatrix}, \tag{20}$$

$$\bar{\mathbf{C}} = \begin{pmatrix} \mathbf{0} & \mathbf{0} \\ \mathbf{0} & \mathbf{C}_{\text{qq}} \end{pmatrix}, \tag{21}$$

$$\bar{\mathbf{D}} = \begin{pmatrix} \mathbf{D}_{\text{adm}} & \mathbf{0} \\ \mathbf{0} & \mathbf{D}_{\text{qq}} \end{pmatrix}, \tag{22}$$

$$\boldsymbol{\tau}_{\text{r,q}}^{\text{ext}} = \begin{pmatrix} \boldsymbol{\tau}_{\text{r}}^{\text{ext}} \\ \boldsymbol{\tau}_{\text{q}}^{\text{ext}} \end{pmatrix}. \tag{23}$$

Based on the following continuously differentiable, energy-like storage function one can conclude passivity and asymptotic stability:

$$V(\tilde{\mathbf{x}}, \dot{\mathbf{y}}) = \frac{1}{2}\dot{\mathbf{y}}^T \bar{\mathbf{M}}\dot{\mathbf{y}} + V_{\text{imp}}(\tilde{\mathbf{x}}) \,. \tag{24}$$

The time derivative yields

$$\dot{V}(\tilde{\mathbf{x}}, \dot{\mathbf{y}}) = \dot{\mathbf{y}}^T \boldsymbol{\tau}_{\text{r,q}}^{\text{ext}} - \dot{\mathbf{y}}^T \bar{\mathbf{D}}\dot{\mathbf{y}} \,. \tag{25}$$

The reason for the beneficial and simple structure of (25) is the modified dynamics (19). The only configuration-dependent submatrix in $\bar{\mathbf{M}}$ is $\mathbf{M}_{\text{qq}} = \mathbf{M}_{\text{qq}}(\mathbf{q})$, which depends on the upper body configuration only. Hence $\mathbf{C}_{\text{qq}} = \mathbf{C}_{\text{qq}}(\mathbf{q}, \dot{\mathbf{q}})$, and the property $\dot{\mathbf{M}}_{\text{qq}} = \mathbf{C}_{\text{qq}} + \mathbf{C}_{\text{qq}}^T$ holds, cf. (2).

If the compensation (17) was not applied in (16), the term (25) would get more complex. Then it would not be possible to conclude any stability properties from (25).

4.2.1 Passivity of the closed loop and LaSalle's invariance principle

Using the storage function $V(\tilde{\mathbf{x}}, \dot{\mathbf{y}})$, one can conclude strict output passivity (van der Schaft 2000) of the closed loop w. r. t. the input $\boldsymbol{\tau}_{\text{r,q}}^{\text{ext}}$ and the output $\dot{\mathbf{y}}$, see Fig. 5. That becomes clear in (25), where $\bar{\mathbf{D}}$ is positive definite.

An undisturbed system ((19) with $\boldsymbol{\tau}_{\text{r,q}}^{\text{ext}} = \mathbf{0}$) is assumed and LaSalle's invariance principle is applied. Since $\dot{V}(\tilde{\mathbf{x}}, \dot{\mathbf{y}})$ is only negative semi-definite, the states $\dot{V}(\tilde{\mathbf{x}}, \dot{\mathbf{y}}) = 0$, based on (25), have to be investigated. For $\dot{\mathbf{y}} = \ddot{\mathbf{y}} = \mathbf{0}$ and $\boldsymbol{\tau}_{\text{r,q}}^{\text{ext}} = \mathbf{0}$, (19) delivers

$$\left(\frac{\partial V_{\text{imp}}(\tilde{\mathbf{x}}(\mathbf{y}))}{\partial \mathbf{y}}\right)^T = \mathbf{0} \tag{26}$$

which only holds for $(\tilde{\mathbf{x}}, \dot{\mathbf{y}}) = (\mathbf{0}, \mathbf{0})$. Hence, one concludes asymptotic stability of this equilibrium.

4.2.2 Robot setup and control task integration

With the insights from the above sections, one has to distinguish between different robot setups and task integrations, determined by the dimension of the operational space n_{x} and the total number of actuated joints. The cases are (i) non-redundant robots ($n_{\text{x}} = n_{\text{r}} + n_{\text{q}}$), (ii) redundant robots ($n_{\text{x}} < n_{\text{r}} + n_{\text{q}}$) where only damping is applied in the null space of the operational space task according to (22), and (iii) redundant systems ($n_{\text{x}} < n_{\text{r}} + n_{\text{q}}$) where further tasks are applied in the null space of the operational space task.

(i) *Non-redundant robot* If $n_{\text{x}} = n_{\text{r}} + n_{\text{q}}$ then the robot is non-redundant w. r. t. the operational space task, no null space exists. Asymptotic stability of the equilibrium can even be shown in the configuration space for the equilibrium $(\mathbf{y}^*, \dot{\mathbf{y}})$ with $\tilde{\mathbf{x}}(\mathbf{y}^*) = \mathbf{0}$ and $\dot{\mathbf{y}} = \mathbf{0}$.

(ii) *Redundant robot with null space damping* If $n_{\text{x}} < n_{\text{r}} + n_{\text{q}}$ then the robot is redundant w. r. t. the operational space task, a null space exists. If the control law (16) is applied, the overall damping matrix (22) is positive definite, thus the damping also covers the null space of the operational space task. Passivity and asymptotic stability of the equilibrium $(\tilde{\mathbf{x}}(\mathbf{y}^*), \dot{\mathbf{y}}) = (\mathbf{0}, \mathbf{0})$ can be shown. The joint configuration $\mathbf{y}^*$ cannot be determined because the null space configuration is not unique.

(iii) *Redundant robot with further null space tasks* If $n_{\text{x}} < n_{\text{r}} + n_{\text{q}}$ then the robot is redundant w. r. t. the operational space task, a null space exists. In order to properly define the null space behavior also on position level, priority-based control concepts can be applied. The complete stability analysis of this case goes beyond the scope of this paper. But the present system has the same structure as the one in our recent work (Dietrich et al. 2013). Thus, the stability analysis (Dietrich et al. 2013) fully applies to the case investigated here. In short, dynamic consistency within the task hierarchy is implemented (Khatib 1987; Dietrich et al. 2015) and the tasks are decoupled in a way such that conditional stability theory (van der Schaft 2000) can be successively applied to each hierarchy level to show asymptotic stability of the overall, priority-consistent equilibrium $(\mathbf{y}^*, \dot{\mathbf{y}})$ with $\dot{\mathbf{y}} = \mathbf{0}$.

5 Experiments

The control law is validated on the humanoid robot Rollin' Justin following the structure in Fig. 5. The control gains are set according to Table 3, where the Cartesian stiffness matrix $\mathbf{K}$ is split up into its translational part $\mathbf{K}_{\text{transl}}$ and

Table 3 Parameters for the experiments on Rollin' Justin

Gain	Value
$\mathbf{M}_{\text{adm}}$	diag(7.5 kg, 7.5 kg, 2.5 kg m^2)
$\mathbf{D}_{\text{adm}}$	diag(24 kg/s, 24 kg/s, 8 kg m^2/s)
$\mathbf{K}_{\text{transl}}$	diag(1000 N/m, 1000 N/m, 1000 N/m)
$\mathbf{K}_{\text{rot}}$	diag(100 Nm/rad, 100 Nm/rad, 100 Nm/rad)
$\mathbf{D}_{\text{qq}}$	$\boldsymbol{\xi} = (0.7, 0.7, 0.7, 0.7, 0.7, 0.7)$

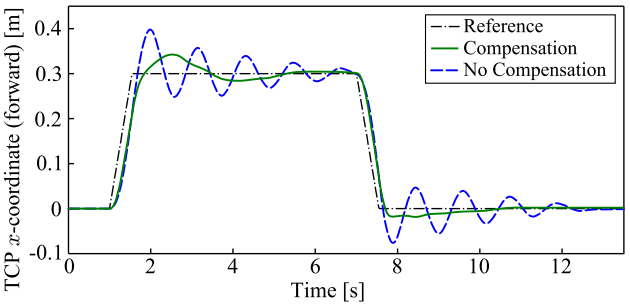

Fig. 6 Comparison of the TCP behavior in forward direction

rotational part $\mathbf{K}_{\text{rot}}$. The upper body damping matrix $\mathbf{D}_{\text{qq}}$ is configuration-dependent in order to realize damping ratios $\boldsymbol{\xi}$ related to a desired mass-spring-damper relation at the TCP. This so-called Double Diagonalization approach is further explained in Albu-Schäffer et al. (2003). The following serial kinematic chain is considered for Rollin' Justin: 3 DOF in the Cartesian directions of the mobile base, 4 DOF in the torso joints (3 active, 1 passive), and 7 DOF in the right arm. Thus 13 DOF are actuated in total. Furthermore an impedance in the torso is applied to keep it within feasible regions in the body frame, a self-collision avoidance (Dietrich et al. 2011b, 2012a) is applied, and a singularity avoidance for the arm is activated in the null space of the Cartesian impedance of the TCP to optimize the manipulability. These additional subtasks have already been applied in our previous works (Dietrich et al. 2011a, 2012b) in order to exploit the high degree of kinematic redundancy in Rollin' Justin.

In the first experiment, a continuous forward trajectory of length 0.3 m is commanded to the right TCP. The transient spatial behavior of the TCP is shown in Fig. 6. With compensation, a nice impedance behavior is achieved with small overshooting. This is due to two reasons: first, the damping ratio for the Cartesian impedance is set to 0.7, cf. Table 3, which is a standard parameterization for this kind of lightweight robot (Albu-Schäffer et al. 2003) that leads to a fast response at the cost of small overshoots. Second, the kinematic velocity controller of the mobile base does not ensure $\dot{\mathbf{r}} = \dot{\mathbf{r}}^{\text{des}}$. The introduced phase delay inevitably leads to slight uncertainties in the model such that the formulation (9) does not perfectly match the real dynamics. Without compensation, the system oscillates significantly

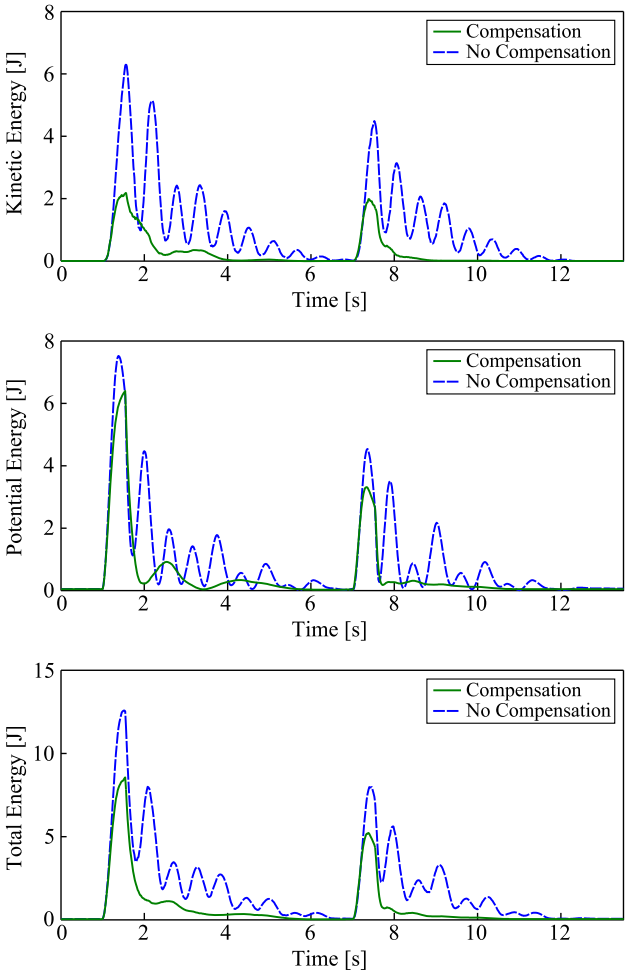

Fig. 7 Kinetic energy, potential energy, and the sum of both in experiments with and without compensation

and takes a relatively long time to reach a steady state. However, by applying the chosen parameterization the system still remains stable, even without compensation. Note that we have chosen these gains for a proper comparison of the performances between active and inactive compensation. If the admittance mass and damping were further reduced, instability would result without compensation of the inertia and Coriolis/centrifugal couplings. Such a scenario will be shown in the last experiment and in the video.

In terms of the stability properties, the energy (24) is of interest as well.[2] The top plot in Fig. 7 depicts the kinetic energies based on the admittance inertia. In case of uncompensated inertia and Coriolis/centrifugal couplings, there are large oscillations whose extent cannot be observed in the TCP deviation in Fig. 6 alone. The potential energy part of

[2] Equation (24) does not match the real physical energy due to the use of the admittance inertia instead of the real one. An overall potential energy including the other subtasks is not meaningful due to the null space projections (Dietrich et al. (2013)).

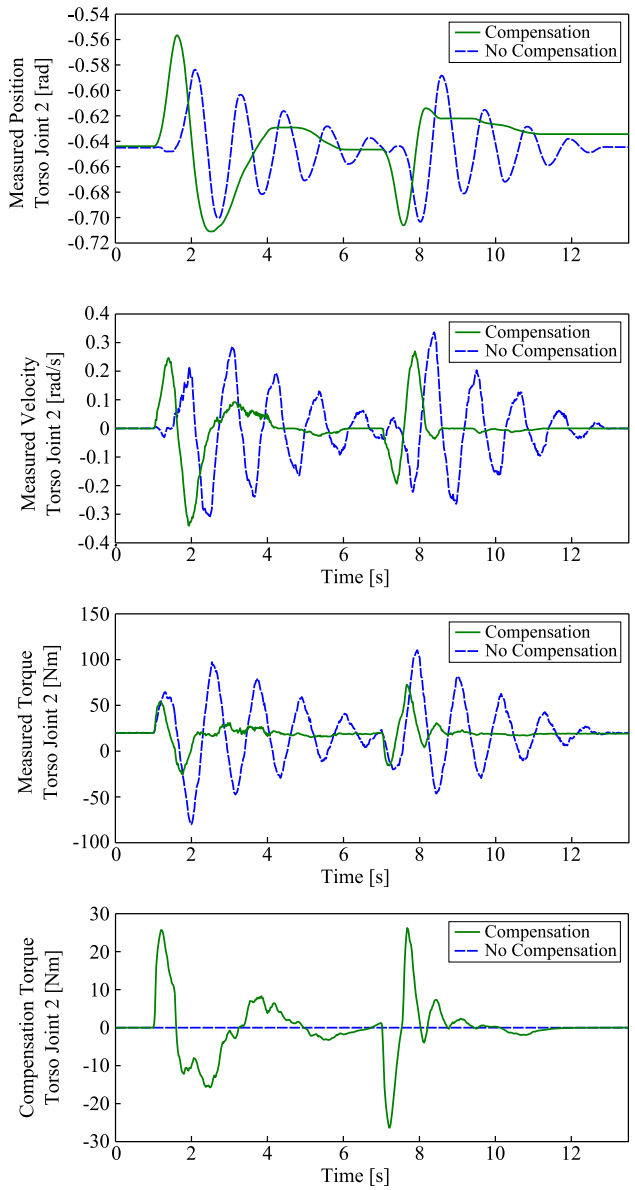

Fig. 8 Joint values, velocities, and torques in the second torso joint. The axis of this joint lies in the *horizontal plane* and is responsible for motions about the pitch axis

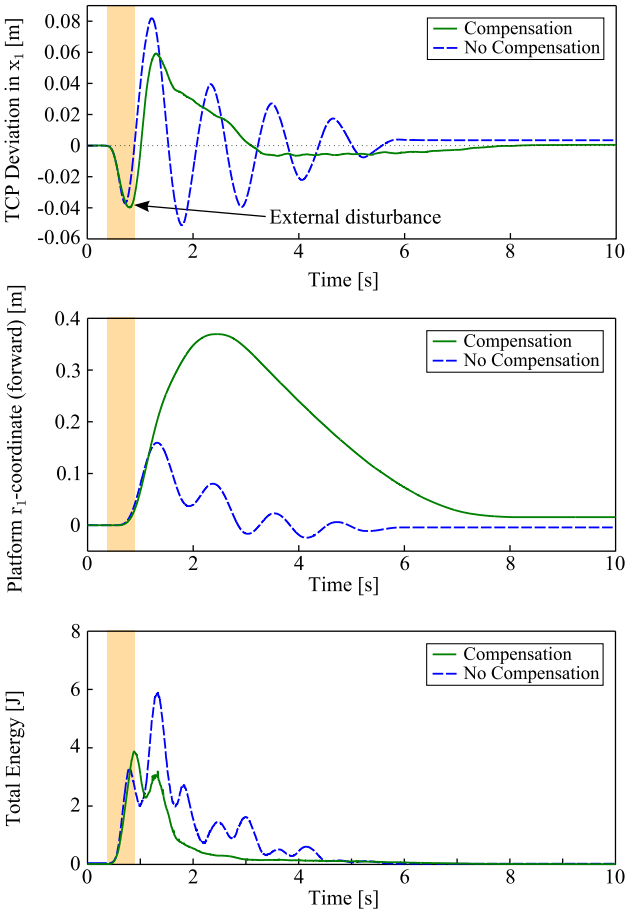

Fig. 9 Physical human–robot interaction: the robot is disturbed during the marked time period

(24) is shown in the center diagram of Fig. 7. The sum of the kinetic and the potential energy is given in the bottom chart of Fig. 7. The stability problems without compensation become obvious here as well. To get an insight into the behavior on joint level, Fig. 8 has been recorded. In the first two charts the joint values and velocities of the second torso joint are plotted for comparison. One can clearly see the differences due to the compensation term. Note that this axis is responsible for pitch motions and located directly above the mobile base. Hence only small motions in this joint have a massive impact on the TCP pose due to the long lever arm. On joint torque level (third diagram in Fig. 8), large oscillations can be observed in case of uncompensated inertia and Coriolis/centrifugal couplings. In contrast, when they are compensated, only the inevitable peaks during the acceleration and deceleration phase are noteworthy in the plot. The bottom chart in Fig. 8 shows the actual compensation torque in this specific joint.

In the next experiment, the compliance behavior is investigated and the parameters from Table 3 are used again. A human disturbs the robot by moving the TCP away from the desired equilibrium about 4 cm, see Fig. 9 (top). During that time, the mobile base starts to accelerate to compensate for the error, see Fig. 9 (center). When abruptly releasing the end-effector again, the TCP error converges properly in case of active compensation. If deactivated, massive oscillations can be observed in the error plots. When comparing the base position, one can clearly see that the platform changes its moving direction repeatedly, while it shows a proper behavior in case of activated compensation. The coordination between upper body and mobile base is reasonable. While the platform is still moving backwards ($3\,\mathrm{s} < t < 8\,\mathrm{s}$) from about $r_1 \approx 0.3\,\mathrm{m}$, the TCP error is already very small with less than 1 cm. The total energy based on the admittance mass/inertia and velocity is plotted in Fig. 9 (bottom). The short-time

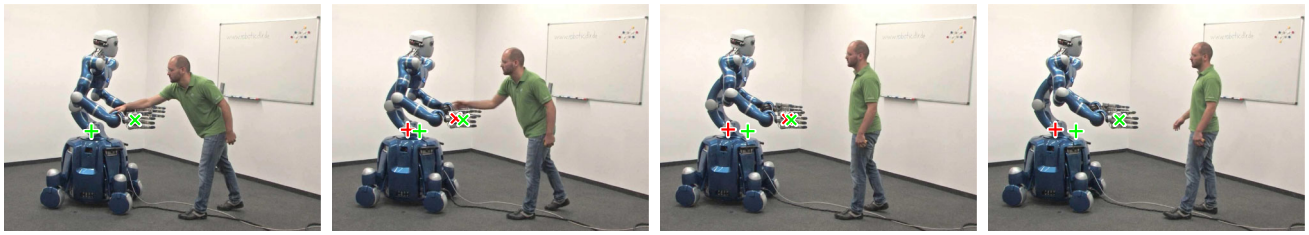

(a) $t = 0\,\mathrm{s}$ **(b)** $t = 0.5\,\mathrm{s}$ **(c)** $t = 1\,\mathrm{s}$ **(d)** $t = 1.5\,\mathrm{s}$

Fig. 10 Snapshots from experiments on Rollin' Justin with active inertia and Coriolis/centrifugal decoupling. The platform admittance is parameterized with $\mathbf{M}_{\mathrm{adm}} = \mathrm{diag}(3\,\mathrm{kg}, 3\,\mathrm{kg}, 1\,\mathrm{kg\,m^2})$, $\mathbf{D}_{\mathrm{adm}} = \mathrm{diag}(21\,\mathrm{kg/s}, 21\,\mathrm{kg/s}, 7\,\mathrm{kg\,m^2/s})$. The *green plus symbol* (+) indicates the initial platform position. The *green cross* (×) indicates the initial and desired position of the right TCP. The *red plus* symbol depicts the actual platform position, and the *red cross* represents the actual TCP position of the right arm (Color figure online)

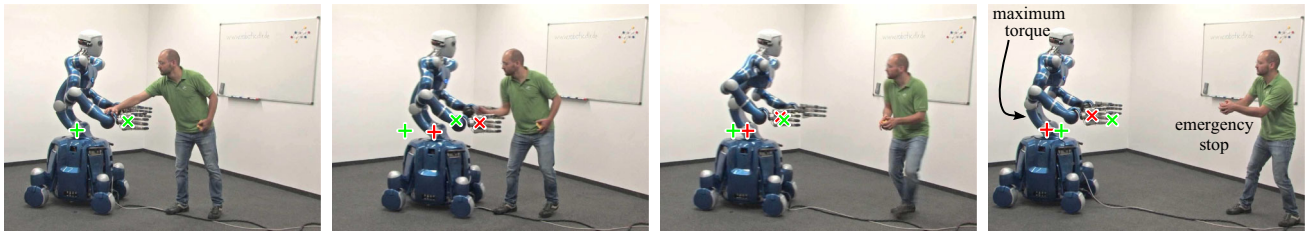

(a) $t = 0\,\mathrm{s}$ **(b)** $t = 0.5\,\mathrm{s}$ **(c)** $t = 1\,\mathrm{s}$ **(d)** $t = 1.5\,\mathrm{s}$

Fig. 11 Snapshots from experiments on Rollin' Justin with inactive inertia and Coriolis/centrifugal decoupling. The platform admittance is parameterized with $\mathbf{M}_{\mathrm{adm}} = \mathrm{diag}(3\,\mathrm{kg}, 3\,\mathrm{kg}, 1\,\mathrm{kg\,m^2})$, $\mathbf{D}_{\mathrm{adm}} = \mathrm{diag}(21\,\mathrm{kg/s}, 21\,\mathrm{kg/s}, 7\,\mathrm{kg\,m^2/s})$. The *green plus symbol* (+) indicates the initial platform position. The *green cross* (×) indicates the initial and desired position of the right TCP. The *red plus* symbol depicts the actual platform position, and the *red cross* represents the actual TCP position of the right arm (Color figure online)

increase in the energy (for activated compensation) at about $1\,\mathrm{s} < t < 1.5\,\mathrm{s}$ can be traced back to the performance of the velocity controller for the mobile base and the resulting model uncertainties in (19). It should be mentioned that the magnitude of the platform motion (Fig. 9, center) can be actively influenced, e. g. by increasing the virtual platform mass/inertia to make it move less. Moreover, one can define the null space of the end-effector task, e. g. by applying an impedance-based motion trajectory for the mobile base in order to specify the platform behavior.

In the last experiment, a critical set of parameters for the admittance is chosen so that instability finally occurs:

$$\mathbf{M}_{\mathrm{adm}} = \mathrm{diag}(3\,\mathrm{kg}, 3\,\mathrm{kg}, 1\,\mathrm{kg\,m^2})\,,$$
$$\mathbf{D}_{\mathrm{adm}} = \mathrm{diag}(21\,\mathrm{kg/s}, 21\,\mathrm{kg/s}, 7\,\mathrm{kg\,m^2/s})\,.$$

Note that the mobile base has a nominal mass of about 150 kg. In other words, the velocity controller is instructed to reduce the perceived inertia to only 2 % of the original value. Moreover, the platform has to accelerate and decelerate the upper body of about 45 kg additionally. Figure 10 shows the experiment with active compensation of the inertia and Coriolis/centrifugal couplings. While the user is pulling the robot at the right end-effector, the reactive whole-body controller is compensating for the introduced Cartesian TCP deviation by moving backwards. After releasing the end-effector again, the virtual equilibrium of the TCP is reached fast by exploiting the kinematic redundancy in the upper body. The whole transient only takes about 1.5 s.

Figure 11 shows the same scenario without compensation. Only slightly touching the end-effector immediately destabilizes the system. Notice that within only 1.5 s, i. e. between Fig. 11a and 11d, the platform moves a great distance forward (Fig. 11b) and backward (Fig. 11c, d). At $t = 1.5\,\mathrm{s}$, the operator uses the emergency stop due to the large kinetic energy in the system. Furthermore, at $t = 1.5\,\mathrm{s}$ the maximum permissible torque in the first horizontal torso axis (pitch motion) of 230 Nm is reached.

6 Discussion

The controller shapes the overall dynamics by modifying the inertia matrix and the Coriolis/centrifugal terms. It is natural to question whether such an intervention causes problems in terms of robustness and availability of measurements. Cancelling parts of the Coriolis and centrifugal matrix requires model-based calculations but only positions and velocities are used in the feedback law. These signals are usually measured or can be derived by differentiating w. r. t. time without jeopardizing the robustness. The same applies to damping

injection (14). An issue is the modification of the inertia matrix since acceleration measurements have to be available. However, the respective term in (17) only requires the Cartesian base accelerations. These signals can be taken from (3) without resorting to any additional measurements or differentiations w. r. t. time due to the assumption $\dot{\mathbf{r}} \approx \dot{\mathbf{r}}^{\mathrm{des}}$ made in Sect. 3.1. Summarized, there are no critical issues in the proposed control concept as also observed during the experiments on Rollin' Justin.

The high performance of the platform velocity controller, which extinguishes any disturbances (cf. Fig. 2), is an assumption made in the stability analysis. Naturally, there will be a difference between the assumed, *ideal* closed-loop system model and the actual dynamics. In order to further close the gap between these two, one could consider implementing a disturbance observer such as Ohnishi et al. (1996) to improve the performance of the motion control of the platform. In fact, during the experiments we have experienced that the velocity control of the platform does not work perfectly but it introduces a phase delay. Nevertheless, we did not encounter any stability problems during the experiments related to these model uncertainties. From that perspective, the assumption is justified on Rollin' Justin.

Another aspect of the implementation is the knowledge of the dynamic parameters which are used in the feedback. Equation (9) can be computed in a straightforward way with symbolic algebra programs. The wheel dynamics are disregarded and the platform admittance (achieved via the kinematic control) is assumed to be part of the computed dynamics.

A further issue addresses the external forces/torques exerted on the mobile base. In (3) they are used in the admittance simulation. In order to provide interaction compliance also with respect to external forces/torques exerted there, measurements have to be performed. If no sensors are available, this feedback is set to zero and exerted external forces/torques will not lead to compliant behavior in the platform. The velocity controller of the mobile base will compensate for these disturbances as indicated in Fig. 2. Currently, Rollin' Justin is not equipped with such sensors.

The proposed whole-body impedance controller can be used for complex tasks such as household chores. Recently we have presented a service application, where Rollin' Justin cleaned a large window (Leidner et al. 2014). However, in that work the complete planning has been performed in the high-dimensional configuration space, which is computationally not efficient and very time-consuming in the planning step. With the controller proposed here, we are able to do the planning in a dramatically reduced space such as the Cartesian space of the end-effector which carries the window wiper. A combination of Leidner et al. (2014) with the work proposed here is expected to unite the benefits of hybrid reasoning (global solutions in the planning) and compliant behavior in terms of the whole-body impedance (local, reactive behavior).

The field of application of the presented whole-body impedance is not restricted to wheeled robots in principle. If the motion of the mobile base is accessible, be it a wheeled, legged, or flying system, then the approach can be used. In general, the proposed controller can be applied to any system with motion-controlled mobile base and force-torque-controlled manipulator mounted on it.

7 Conclusions

We have presented a whole-body impedance controller for wheeled mobile humanoids with torque-controlled upper body. As such systems usually have nonholonomic mobile platforms, the kinematic rolling constraints have to be considered in the control of the base. Hence the platform systems are mostly kinematically controlled. A compliant whole-body behavior based on impedance laws can yet be applied by using an admittance interface to the mobile base. Additionally, that way one can reduce the apparent platform inertia to obtain a humanoid robot consisting of subsystems (arms, torso, platform) with similar inertial properties. The controller proposed here takes these aspects into account and deals with structural stability issues which arise when combining torque control (upper body) with admittance control (mobile platform). The control scheme allows a formal proof of stability based on strict output passivity in the operational space that features asymptotic stability of the desired equilibrium. Experiments on the humanoid robot Rollin' Justin validated the approach. Possible applications for the method are service tasks where compliant behavior is desired, safety is required, and the planning is to be performed in a low-dimensional task space instead of considering the complete configuration space of the robot.

References

Albu-Schäffer, A., Ott, C., Frese, U., & Hirzinger, G. (2003). Cartesian Impedance control of redundant robots: Recent results with the DLR-Light-Weight-Arms. In *Proceedings of the 2003 IEEE International Conference on Robotics and Automation* (pp. 3704–3709).

Albu-Schäffer, A., Ott, C., & Hirzinger, G. (2007). A unified passivity-based control framework for position, torque and impedance control of flexible joint robots. *International Journal of Robotics Research*, *27*(1), 23–39.

Asfour, T., Regenstein, K., Schröder, J., Bierbaum, A., Vahrenkamp, N., & Dillmann, R. (2006). ARMAR-III: An integrated humanoid platform for sensory-motor control. In *Proceedings of the 6th IEEE-RAS International Conference on Humanoid Robots* (pp. 169–175).

Bohren, J., Rusu, R.B., Jones, E.G., Marder-Eppstein, E., Pantofaru, C., Wise, M., Mösenlechner, L., Meeussen, W., & Holzer, S. (2011).

Towards autonomous robotic butlers: Lessons learned with the PR2. In *Proceedings of the 2011 IEEE International Conference on Robotics and Automation* (pp. 5568–5575).

Borst, C., Wimböck, T., Schmidt, F., Fuchs, M., Brunner, B., Zacharias, F., Giordano, P.R., Konietschke, R., Sepp, W., Fuchs, S., Rink, C., Albu-Schäffer, A., & Hirzinger, G. (2009). Rollin' Justin—Mobile platform with variable base. In *Proceedings of the 2009 IEEE International Conference on Robotics and Automation* (pp. 1597–1598).

Campion, G., Bastin, G., & D'Andréa-Novel, B. (1996). Structural properties and classification of kinematic and dynamic models of wheeled mobile robots. *IEEE Transactions on Robotics and Automation*, *12*(1), 47–62.

Connette, C.P., Pott, A., Hägele, M., & Verl, A. (2008). Control of an Pseudo-omnidirectional, non-holonomic, mobile robot based on an ICM representation in spherical coordinates. In *Proceedings of the 47th IEEE Conference on Decision and Control* (pp. 4976–4983).

Dietrich, A., Ott, C., & Albu-Schäffer, A. (2013). Multi-objective compliance control of redundant manipulators: Hierarchy, control, and stability. In *Proceedings of the 2013 IEEE/RSJ International Conference on Intelligent Robots and Systems* (pp. 3043–3050).

Dietrich, A., Ott, C., & Albu-Schäffer, A. (2015). An overview of null space projections for redundant, torque-controlled robots. *International Journal of Robotics Research*. doi:10.1177/0278364914566516.

Dietrich, A., Wimböck, T., & Albu-Schäffer, A. (2011). Dynamic whole-body mobile manipulation with a torque controlled humanoid robot via impedance control laws. In *Proceedings of the 2011 IEEE/RSJ International Conference on Intelligent Robots and Systems* (pp. 3199–3206).

Dietrich, A., Wimböck, T., Albu-Schäffer, A., & Hirzinger, G. (2012). Integration of reactive, torque-based self-collision avoidance into a task hierarchy. *IEEE Transactions on Robotics*, *28*(6), 1278–1293.

Dietrich, A., Wimböck, T., Albu-Schäffer, A., & Hirzinger, G. (2012). Reactive whole-body control: Dynamic mobile manipulation using a large number of actuated degrees of freedom. *IEEE Robotics & Automation Magazine*, *19*(2), 20–33.

Dietrich, A., Wimböck, T., Täubig, H., Albu-Schäffer, A., & Hirzinger, G. (2011). Extensions to reactive self-collision avoidance for torque and position controlled humanoids. In *Proceedings of the 2011 IEEE International Conference on Robotics and Automation* (pp. 3455–3462).

Giordano, P.R., Fuchs, M., Albu-Schäffer, A., & Hirzinger, G. (2009). On the kinematic modeling and control of a mobile platform equipped with steering wheels and movable legs. In *Proceedings of the 2009 IEEE International Conference on Robotics and Automation* (pp. 4080–4087).

Hogan, N. (1985). Impedance control: An approach to manipulation: Part I—theory, part II—implementation, part III—applications. *Journal of Dynamic Systems, Measurement, and Control*, *107*, 1–24.

Iwata, H., & Sugano, S. (2009). Design of human symbiotic robot TWENDY-ONE. In *Proceedings of the 2009 IEEE International Conference on Robotics and Automation* (pp. 580–586).

Kaneko, K., Kanehiro, F., Morisawa, M., Akachi, K., Miyamori, G., Hayashi, A., & Kanehira, N. (2011). Humanoid Robot HRP-4—Humanoid robotics platform with lightweight and slim body. In *Proceedings of the 2011 IEEE/RSJ International Conference on Intelligent Robots and Systems* (pp. 4400–4407).

Khatib, O. (1987). A unified approach for motion and force control of robot manipulators: The operational space formulation. *IEEE Journal of Robotics and Automation*, *RA–3*(1), 43–53.

Khatib, O., Sentis, L., Park, J., & Warren, J. (2004). Whole-body dynamic behavior and control of human-like robots. *International Journal of Humanoid Robotics*, *1*(1), 29–43.

Leidner, D., Dietrich, A., Schmidt, F., Borst, C., & Albu-Schäffer, A. (2014). Object-centered hybrid reasoning for whole-body mobile manipulation. In *Proceedings of the 2014 IEEE International Conference on Robotics and Automation* (pp. 1828–1835).

Lohmeier, S., Buschmann, T., & Ulbrich, H. (2009). Humanoid robot LOLA. In *Proceedings of the 2009 IEEE International Conference on Robotics and Automation* (pp. 775–780).

Moro, F.L., Gienger, M., Goswami, A., Tsagarakis, N.G., & Caldwell, D.G. (2013). An Attractor-based Whole-Body Motion Control (WBMC) System for humanoid robots. In *Proceedings of the 13th IEEE-RAS International Conference on Humanoid Robots* (pp. 42–49).

Murray, R. M., Li, Z., & Sastry, S. S. (1994). *A mathematical introduction to robotic manipulation*. Boca Raton, FL: CRC Press.

Nagasaka, K., Kawanami, Y., Shimizu, S., Kito, T., Tsuboi, T., Miyamoto, A., Fukushima, T., & Shimomura, H. (2010). Whole-body cooperative force control for a two-armed and two-wheeled mobile robot using generalized inverse dynamics and idealized joint units. In *Proceedings of the 2010 IEEE International Conference on Robotics and Automation* (pp. 3377–3383).

Ohnishi, K., Shibata, M., & Murakami, T. (1996). Motion control for advanced mechatronics. *IEEE/ASME Transactions on Mechatronics*, *1*(1), 56–67.

Ott, C. (2008). Cartesian impedance control of redundant and flexible-joint robots. *Springer tracts in advanced robotics* (Vol. 49). Berlin: Springer.

Sakagami, Y., Watanabe, R., Aoyama, C., Matsunaga, S., Higaki, N., & Fujimura, K. (2002). The intelligent ASIMO: System overview and integration. In *Proceedings of the 2002 IEEE/RSJ International Conference on Intelligent Robots and Systems* (pp. 2478–2483).

Sentis, L., & Khatib, O. (2005). Synthesis of whole-body behaviors through hierarchical control of behavioral primitives. *International Journal of Humanoid Robotics*, *2*(4), 505–518.

Siciliano, B., & Khatib, O. (2008). *Springer handbook of robotics*. Berlin: Springer.

Stilman, M., Olson, J., & Gloss, W. (2010). Golem Krang: Dynamically stable humanoid robot for mobile manipulation. In *Proceedings of the 2010 IEEE International Conference on Robotics and Automation* (pp. 3304–3309).

Thuilot, B., D'Andréa-Novel, B., & Micaelli, A. (1996). Modeling and feedback control of mobile robots equipped with several steering wheels. *IEEE Transactions on Robotics and Automation*, *12*(3), 375–390.

van der Schaft, A. (2000). *L_2-Gain and passivity techniques in nonlinear control* (2nd ed.). Berlin: Springer.

van Ham, R., Sugar, T. G., Vanderborght, B., Hollander, K. W., & Lefeber, D. (2009). Compliant actuator designs: Review of actuators with passive adjustable compliance/controllable stiffness for robotic applications. *IEEE Robotics & Automation Magazine*, *16*(3), 81–94.

Alexander Dietrich received his Dipl.-Ing. degree in mechanical engineering with focus on control theory and fundamentals in engineering sciences from the Technische Universität München (TUM) in 2008. In 2010, he joined the German Aerospace Center (DLR), Institute of Robotics and Mechatronics, as a research scientist. His current research interests include impedance and force control, whole-body mobile manipulation, kinematic redundancy, and safe physical human–robot interaction.

Kristin Bussmann received her M.Sc. degree in mechanical engineering with focus on control theory and information technology from the Technische Universität München (TUM) in 2014. In the same year, she joined the German Aerospace Center (DLR), Institute of Robotics and Mechatronics, as a research assistant. Her current research interests include nonholonomic systems and mobile manipulation.

Florian Petit received the Dipl.-Ing. degree in Electrical Engineering from the Technical University of Munich, Munich, Germany, in 2008. He joined the Institute of Robotics and Mechatronics, German Aerospace Center, Wessling, Germany, in 2009. He has also been a member of the Sensory-Motor Systems Laboratory, Swiss Federal Institute of Technology Zurich, Zurich, Switzerland, since 2012. His research interests include variable impedance robots and control, impedance and force control, and nonlinear systems and control.

Paul Kotyczka received the Dipl.-Ing. degree in Electrical Engineering and information technology and the Dr.-Ing. degree in automatic control from Technische Universität München (TUM) in 2005 and 2010, respectively. Since 2011 he has been Akademischer Rat (assistant professor) at the Institute of Automatic Control (Prof. Boris Lohmann) at TUM, where he leads the energy based modeling and control group. His main research interests are in the field of physical modeling and energy based nonlinear control, with applications to mechanical and infinite-dimensional systems.

Christian Ott received his Dipl.-Ing. degree in mechatronics from the Johannes Kepler University (JKU), Linz, Austria, in 2001 and his Ph.D. (Dr.-Ing.) degree from Saarland University, Saarbruecken, Germany, in 2005. From March 2001 to April 2007, he was with the German Aerospace Center (DLR e.V.), Institute of Robotics and Mechatronics, Wessling, Germany. From August to Oktober 2003, he was a visiting researcher at the University of Twente, The Netherlands. From May 2007 to May 2009, he has been working as a Project Assistant Professor in the Department of Mechano-Informatics, University of Tokyo, Japan. Since June 2009, he works as a senior researcher at the German Aerospace Center (DLR e.V.), Institute of Robotics and Mechatronics. His research interests include nonlinear control of robotic systems, flexible joint robots, impedance control, two-armed (humanoid) manipulation, and biped locomotion.

Boris Lohmann is the head of the Institute of Automatic Control of the Faculty of Mechanical Engineering at TU München. His fields of research include nonlinear, robust, and optimal control, active vibration control, model order reduction, and applications in robotics and automotive.

Alin Albu-Schäffer (M'93) received the Diploma degree in Electrical Engineering from the Technical University of Timisoara, Timisoara, Romania, in 1993 and the Ph.D. degree in control systems from the Technical University of Munich, Munich, Germany, in 2002. Since 2012, he has been Head of the Institute of Robotics andMechatronics, German Aerospace Center, Wessling, Germany, which he joined in 1995. His research interests include robot design, modeling, and control, nonlinear control, flexible joint and variable compliance robots, impedance and force control, and physical human–robot interaction.